Comparing several spectral methods used to extract displacement fields from checkerboard images

Michel Grediac, Benoît Blaysat, Frédéric Sur

Comparing several spectral methods used to extract displacement fields from checkerboard images

Michel Grédiac[1], Benoît Blaysat[1], Frédéric Sur[2]

[1] *Université Clermont Auvergne, CNRS, SIGMA Clermont, Institut Pascal, F-63000 Clermont-Ferrand, France*

[2] *Laboratoire Lorrain de Recherche en Informatique et ses Applications, UMR CNRS 7503 Université de Lorraine, CNRS, INRIA, Campus Scientifique, BP 239, 54506 Vandoeuvre-lès-Nancy Cedex, FRANCE*

Abstract

Checkerboard represents the best pattern for in-plane displacement measurement in terms of sensor noise propagation because this pattern maximizes image gradient. It also exhibits other interesting properties in terms of pattern-induced bias for instance. Digital Image Correlation (DIC) is not the best option to extract displacement fields from such periodic patterns, and spectral methods should be used instead. In this paper, it is shown that three different spectral techniques initially developed for classic bidimensional grids can be adapted to process checkerboard images. These three techniques are the Geometric Phase Analysis (GPA), the windowed version of the Geometric Phase Analysis (WGPA), and the Localized Spectrum Analysis (LSA), which can be regarded as the ultimate version of WGPA. The main features of these three techniques as well as the link between them are given in this paper. Their metrological performance are compared in terms of displacement resolution, spatial resolution and bias. Synthetic checkerboard images deformed with a suitable reference displacement field are considered for this purpose. It is shown that GPA is the fastest method. According to the metric used in this paper, the best metrological performance is obtained with WGPA with suitable settings. LSA followed by a deconvolution algorithm is just behind, but the calculation time is approximately 10 times lower than that of WGPA for the examples considered in this paper, which makes it a reasonable choice for the determination of in-plane displacement fields from checkerboard images.

This is the author-manuscript version of

1 Introduction

Full-field measurement techniques are now widespread in the experimental mechanics community. Digital Image Correlation (DIC), which consists in iteratively minimizing the optical residual over small subsets with respect to the sought displacement, is the most popular one. Finding optimal patterns to achieve the best possible metrological performance is a problem, which has attracted much attention in recent papers [1, 2, 3]. In [3], it is recalled that checkerboards are theoretically optimal patterns for DIC in terms of sensor noise propagation because their images maximize the sum of square of subset intensity gradient (SSSIG), and noise in final displacement and strain maps is inversely proportional to this quantity [4, 5]. This conclusion is drawn if the nearest neighbor forward difference scheme (and not the central difference scheme) is used to numerically estimate the gradient [3, 6]. In [7], it is also shown that checkerboards, as other periodic patterns [8], induce lower pattern-induced bias than random speckles usually employed with DIC. Checkerboards are however quasi-periodic patterns and as such, they cannot be processed by DIC, except if the iterative minimization starts close to the solution to avoid convergence toward a local minimum [6], or if displacement continuity is enforced from a given point where the displacement can be considered as reliable. Consequently, checkerboards are optimal but not easily manageable (if not unmanageable) patterns for DIC in practice. It means that researchers involved in optimal pattern definition for DIC consider additional constraints involving for instance the auto-correlation peaks of the random pattern [3]. This also means that they deliberately deviate from the optimal solution with respect to noise propagation alone, which is the checkerboard and not any random pattern. DIC is however nothing but a numerical procedure developed to iteratively minimize the optical residual over small zones (the subsets) in the spatial domain. It has been demonstrated in [9] that this minimization problem can be advantageously switched to the Fourier domain if the pattern is quasi-periodic, as checkerboards are. In this case, this minimization problem has indeed a unique and straightforward solution, which is given by the following equation classically employed to retrieve displacement fields from grid images:

$$u_i = -\frac{p}{2\pi} \left(\Phi_i^{cur}(x + u_x, y + u_y) - \Phi_i^{ref}(x, y) \right) \quad i \in \{x, y\}. \tag{1}$$

In this equation, p is the pitch of the periodic pattern, Φ_i^{ref} and Φ_i^{cur}, $i \in \{x, y\}$, are the phase distributions of this periodic pattern in the reference and current configurations, respectively.

In [10], it is shown how to process classic 2D grids in order to extract displacement and strain fields from classic 2D images by using the so-called Localized Spectrum Analysis (LSA). In particular, it can be seen in Equation 1 that u_x and u_y are involved in both sides of the equality, so a fixed-point algorithm can be used to find these two quantities. LSA has been adapted in [11] to extract the same information from checkerboard images instead of grid images. The method consists in considering the ± 45 deg directions with respect to the natural directions of a checkerboard (these natural directions are denoted by x and y in the following). In other words these directions are defined by the diagonal of the black and white squares forming a checkerboard. The phases along these diagonals are extracted and the displacement along the x and y-directions are then deduced by applying successively Equation 1 and a change of basis. In [11, 6], it is also experimentally verified that displacement and strain fields extracted from checkerboard images are less noisy than

their counterparts obtained at iso-bias and iso-spatial resolution, either from 2D grid images processed with the same spectral method, [11], or from random speckle images processed by classic subset-based DIC, [6]. In this context, it is of prime importance to check the efficiency of various spectral methods developed hitherto to process 2D grids when they are employed to process the optimal pattern for optical residual minimization, namely the checkerboard. This is the aim of this paper, where three techniques are compared. These techniques are the Geometric Phase Analysis (GPA) [12], the windowed version of GPA (WGPA) [13] and the Localized Spectrum Analysis (LSA) [10]. A fourth technique named sampling moiré has been proposed to process grid images in the recent past [14, 15, 16]. Employing it for checkerboard images seems however not possible. Indeed interpolation between straight lines of the grid is performed with this technique. This is however not possible with checkerboards, the lines of diamonds forming a checkerboard featuring serrated (and not straight) borders.

The paper is organized as follows. The fundamentals of these techniques are first briefly recalled. Synthetic images of checkerboards deformed with a displacement field known *a priori* (and thus considered as a reference) are then considered as input data for these three techniques. The displacement and strain fields obtained with these techniques are finally compared and discussed.

2 Spectral methods to process quasi-periodic images

2.1 Geometric Phase Analysis

Geometric Phase Analysis (GPA) is a technique described first in [12]. In this reference, displacement and strain fields are deduced from high-resolution electron microscope images of regular patterns. These patterns are those of crystal structures observed at the atomic scale. GPA being a purely geometric technique, it has also been used at the macroscopic level to process grid images, [17, 13] for instance. In the present paper, the idea is to use it to retrieve phase maps (and thus subsequent displacement and strain maps) from checkerboard images. We recall first how GPA can be applied to grid images before explaining how to extend the method to checkerboard images.

2.1.1 GPA on grid images

GPA applied to a grid pattern consists first in calculating the Fourier transform of both the reference and the current images. The corresponding spectrograms are filtered in order to select the zone around the spot corresponding to the fundamental frequency of the grid along the first direction along which the in-plane displacement is calculated. This zone is denoted by $\mathcal{Z}_f$ in the following. The procedure is illustrated in Figure 1. A typical grid and the corresponding spectrogram are shown in Figure 1-a and -b, respectively. $\mathcal{Z}_f$ in shown in Figure 1-c. It is then shifted toward the center (not shown in the figure), and the argument of the inverse Fourier transform applied to this spectogram provides the phase distribution modulo 2π. This wrapped phase is unwrapped to obtain the final phase. This procedure is applied for both the x and the y-directions, and the displacement is finally deduced from Equation 1 above. A detailed presentation is available in Appendix 1. An option can be to eliminate the frequencies included in $\mathcal{Z}_f$ whose amplitude is under a certain threshold value because they *a priori* mainly correspond to noise. This procedure limits noise affecting

the phase distribution after taking the inverse Fourier transform. This threshold value is a percentage (denoted here by k) of the magnitude of the peak corresponding to the fundamental frequency, thus of the highest Fourier coefficient of the spot shown in Figure 1-c, which gives Figure 1-d. Note that the effect of noise on the final phase distributions is only limited and not completely avoided, the remaining peaks being also affected by noise.
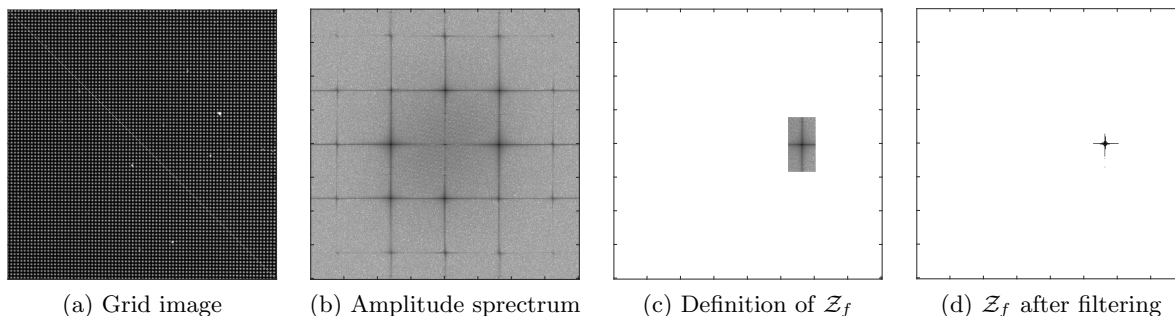

| (a) Grid image | (b) Amplitude sprectrum | (c) Definition of $\mathcal{Z}_f$ | (d) $\mathcal{Z}_f$ after filtering |

Figure 1: Selection of a region $\mathcal{Z}_f$ around the fundamental peak of a grid image in the Fourier domain. (a): Typical grid image. (b): Amplitude spectrum of the grid image. (c) Selection of $\mathcal{Z}_f$. (d): $\mathcal{Z}_f$ after filtering by thresholding the coefficients ($k = 80\%$).

2.1.2 GPA on checkerboard images

Concerning now checkerboards, since the sought displacement is encoded by the phases of the lines of diamonds formed by the ± 45 deg directions, the classic procedure described above must be slightly adapted. A typical checkerboard image and its amplitude spectrum are shown in Figure 2-a and -b, respectively. Spots A or B (only the sign of the phase changes from A to B) correspond to the +45 deg direction and spots C or D correspond to the -45 deg one. The idea is therefore to apply the procedure described above to A or B on the one hand, and to C or D on the other hand, in order to retrieve the phases along the ± 45 deg directions. These phases are then unwrapped and a change of basis is applied to obtain the phases along the x- and y- directions. Equation 1 is finally applied to deduce the displacement.

The quality of the results obtained with GPA depends on two main factors. The first one is the size and shape of the region which is selected around the peak of the spot. The second is the value of k if denoising is applied. Note also that if too many Fourier components are set to 0 (i.e., if k is too large), undesired ringing effect is likely to appear. The influence of these parameters on the results is discussed below with an example.

2.2 Windowed Geometric Phase Analysis

We call here Windowed Geometric Phase Analysis (WGPA) the procedure proposed in [13]. This technique can be considered as a local version of GPA. It consists in focusing on a small zone denoted here by $\mathcal{Z}_r$, which is located around each pixel of the image, and then to apply GPA over each of these zones. $\mathcal{Z}_r$ is generally defined by observing the whole image through a moving window w. $\mathcal{Z}_r$ is defined in the spatial domain and shall not be confused with $\mathcal{Z}_f$ defined in the Fourier domain. $\mathcal{Z}_r$ is then shifted to the next pixel and GPA is applied

(a) Checkerboard image **(b) Amplitude sprectrum** **(c) Definition of $\mathcal{Z}_f$** **(d) $\mathcal{Z}_f$ after filtering**
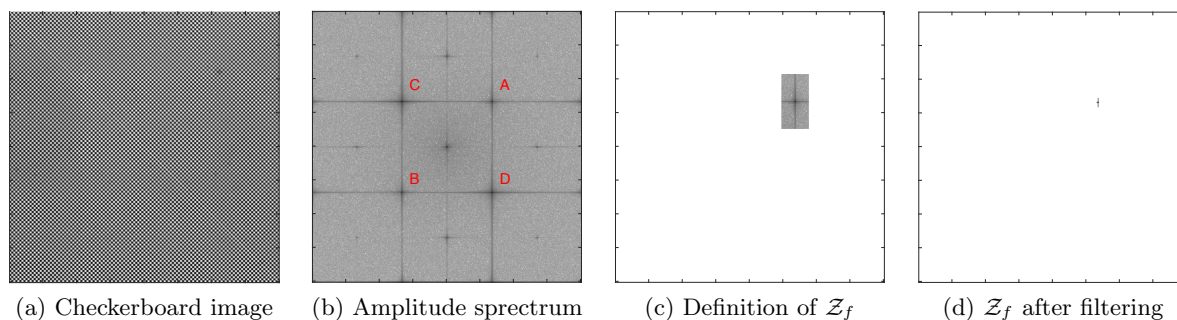
Figure 2: Selection of a region $\mathcal{Z}_f$ around the fundamental peak of a checkerboard image in the Fourier domain. (a): Typical checkerboard image. (b): Amplitude spectrum of the checkerboard image. (c) Selection of $\mathcal{Z}_f$. (d): $\mathcal{Z}_f$ after filtering by thresholding the coefficients ($k = 80\%$).

once again on the new zone. $\mathcal{Z}_r$ is generally defined by a Gaussian envelope over a square whose side is at least equal to three times the standard deviation of the Gaussian. The phase returned by GPA at the center of each zone is considered as the phase at this pixel returned by WGPA. Another option is to consider a weighted average of the phase over the window as the phase returned by WGPA. It has been observed that similar results are obtained in both cases (results not presented here), so only the first option is considered in the present study. As for GPA, the spectrum can be filtered by considering only the Fourier coefficients of the spot higher than a certain threshold value. In [13], it is shown that WGPA is more robust than GPA. The drawback is however to considerably increase the calculation time since GPA is applied in turn for each pixel of the reference and deformed images to retrieve the phases of both images. Compared to GPA applied over the whole image, this induces a significant increase in the computation time, which is not compensated by the fact that with WGPA, GPA is locally applied on sub-images which are much smaller in size than the whole image. Another consequence is that the phase distributions are potentially smoother in the sub-images than in the whole image, which means that the zones around the peaks of the spectrograms *a priori* contain less features and have a simpler shape than their counterparts in the spectrogram of the whole image. Defining the zone around the peaks for GPA and WGPA may therefore obey different rules, as illustrated in the example given in Section 4 below.

2.3 Localized Spectrum Analysis

Derived from algorithms developed for images of temporally phase-shifted fringe patterns [18, 19] and from procedures used to process fringe patterns [20, 21]. The Localized Spectrum Analysis (LSA) is also commonly referred to as the Grid Method in other papers [10]. With the first name, the fact that only one frequency is considered in the Fourier domain is highlighted, but other patterns that classic 2D grids can be processed, which is the case here with checkerboards. With the second name, the fact that classic 2D grids are used is highlighted, but other techniques than LSA such as WGPA or GPA can be used to retrieve the

displacement fields from the images. LSA is also a particular case of WGPA, as explained in detail in Appendix 1. Indeed, instead of applying GPA pixelwise, on small zones $\mathcal{Z}_r$ surrounding each pixel in the spatial domain, and by considering then again small zones $\mathcal{Z}_f$ in the Fourier domain, only one frequency is used for each direction of investigation. This is equivalent to saying that $\mathcal{Z}_f$ reduces to a single point. When classic 2D grids are considered, this is equivalent to a Windowed Fourier Transform performed along each of the two natural axes of symmetry of the grid. The frequency selected along each of the two directions is the nominal frequency of the grid, which corresponds to the highest peak in the $\mathcal{Z}_f$ zone selected in Figure 1-b. LSA can therefore be considered as the ultimate stage of the filtered option of WGPA, since only one frequency component in the Fourier domain is kept for the calculation, the Fourier coefficients corresponding to the other frequencies being all nullified. Various types of windows can be used for the WFT to define $\mathcal{Z}_r$ but it is shown in [22] that a Gaussian envelope corresponds to the best tradeoff between various constraints. When checkerboards are considered, WFT is applied successively along the $\pm$ 45 deg directions, [11]. Compared to LSA applied on classic 2D grids, this is equivalent to WFT applied perpendicularly to the lines of diamonds which can be observed along the diagonals of the checkerboard. The pitch of the checkerboard being denoted by p, the pitch along the lines of diamonds is $p \times \dfrac{\sqrt{2}}{2}$, so the frequency selected when performing WFT is $\dfrac{\sqrt{2}}{p}$ (see Figure 3).
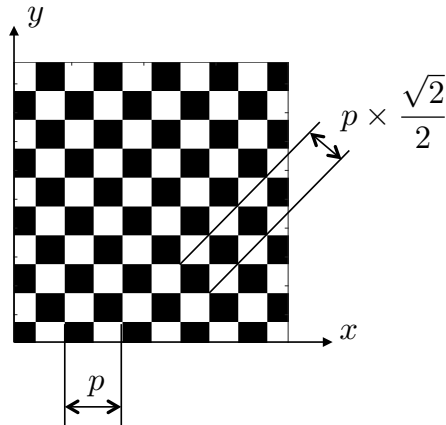

Figure 3: Checkerboard aligned with the $x - y$ axes. Lines of diamonds can easily be observed along the ± 45 deg directions.

An important consequence of using only one frequency with LSA instead of several ones with WGPA is that no inverse WFT shall be applied to the filtered spectrum, as justified in Appendix 1. With LSA, the calculation is therefore limited to two WFTs performed along perpendicular directions. The argument of each WFT is then directly extracted and unwrapped. This avoids applying an inverse Fourier transform on a reduced portion of the spectrogram defined by $\mathcal{Z}_f$, and then extracting the phases. A big advantage of LSA is that the calculation of the WFT becomes here a mere convolution, the argument of which being considered as one of the sought phases. Thanks to the efficiency of the Fast Fourier

Transform, this convolution can be advantageously calculated in the Fourier domain where it becomes then a simple multiplication. This considerably speeds up the calculation of WFT, and subsequently the calculation of the phases and displacements. This property is illustrated in the examples discussed below.

2.4   Convolution/deconvolution

Concerning LSA, an important property is the fact that the phase returned by this technique is not exactly the true phase, but the true phase *convolved* by the window used in the WFT. This result, which holds at the first order, has been demonstrated in [23] in the case of classic grids, but it can easily be extended to checkerboards, as justified in [24]. Convolution causes the amplitude of the details in strain maps to be blurred or, equivalently, causes the Fourier coefficients involved in the discrete Fourier transform of the displacement maps to be lower than their true counterparts. It means that the displacement and strain maps are affected by a systematic error, which depends on the local frequency signature of the true and sought displacement distribution. Measured and true quantities being linked through a convolution, one can theoretically deduce the latter from the former by deconvolving the measurements. Deconvolution is however an ill-posed problem, which makes the solution found very sensitive to noise [25]. It means that some suitable assumptions must be considered while deconvolving noisy strain maps. This is what is proposed in [24], where it is shown that the systematic error due to convolution is cancelled out up to a certain cutoff frequency. The noise is amplified by deconvolution, but in a lower proportion, which means that the total error significantly decreases after deconvolution. In this study, deconvolution will therefore be applied to the results given by LSA. The deconvolution algorithm is briefly described in Appendix 2 for the sake of completeness of the paper. Full details are available in [24].

The results given by GPA and WGPA are not affected by convolution if zone $\mathcal{Z}_r$ selected in the Fourier domain includes the whole spot surrounding the peak corresponding to the frequency of the checkerboard. If this zone is too small and does not contain the whole spot, this automatically induces a convolution of the phase returned by GPA or WGPA, and so the corresponding displacement and strain fields. Note that, in the case of WGPA, convolution may have a spatially varying kernel since the shape of the spot in the Fourier domain potentially changes from one zone of the image to the other, depending on the local displacement field. This point is however not discussed in the literature on GPA and WGPA. The kernel corresponding to this convolution being not identified, deconvolution will not be applied to the results given by GPA or WGPA in the present study.

As a conclusion, Table 1 gives the main features distinguishing the three techniques, which are compared in the present work.

3   Method used to estimate noise and bias in displacement fields obtained with the three techniques

The aim here is to discuss the efficiency of the three techniques recalled above, in other words their ability to reconstruct with the lowest possible error a given displacement field encoded in a deformed checkerboard image. The error discussed here can be split into two different errors, namely the systematic error (or the bias) and the random error. As in recent studies

technique	windowing in the spatial domain	windowing in the Fourier domain	convolution/deconvolution
GPA	no	yes	not applicable
remark	-	*shall include the fundamental peak*	-
WGPA	yes	yes	no (not yet?)
remark	*Gaussian window w*	*shall include the fundamental peak*	*the kernel is not identified and may spatially change*
LSA	yes	yes	yes
remark	*Gaussian window w*	*Dirac at the fundamental peak*	*the kernel is the Gaussian window w*

Table 1: Main differences betweeen GPA, WGPA and LSA.

on the metrological performance of full-field measuring techniques [26], the systematic error considered here is the reduction of the amplitude of the signal returned by the measuring technique for a given frequency. This is precisely the error due to convolution discussed in the preceding section. Other sources of errors such as image distortion also exist but we focus here on the systematic error due to image processing only. The random error in the displacement and strain maps is that due to the image noise. The method used to estimate the systematic and random errors is explained below. Thoroughly estimating the errors means that real images taken during a real test cannot be used. Indeed they would be affected by uncontrolled errors due to experimental conditions, which are extrinsic to the image processing technique itself. In addition, apart from the particular case of a pure translation, the true displacement field would remain unknown in this case, so no reference would be available. We therefore rely here on synthetic checkerboard images, which are artificially deformed with a displacement field which serves then as a reference. A well-controlled heteroscedastic noise is finally added to these images in order to observe and quantify the robustness of each technique.

3.1 Synthetic images suitable for estimating the bias

A synthetic checkerboard image can be easily defined in the x-y plane by using the following function for the gray level distribution:

$$s(x,y) = \frac{A}{2}\left[1 + \sin\left(\frac{2\pi}{p}x + \Phi_x\right)\sin\left(\frac{2\pi}{p}y + \Phi_y\right)\right],\tag{2}$$

where A is a real positive number, fixed here to $A = 2^{12}-1$ to simulate the quantization of the signal with a 12-bit camera sensor. Φ_x and Φ_y are the phases induced by the displacement prescribed along the x- and y-directions. The x- and y-directions correspond to the main directions of the checkerboard. They are aligned with the directions defined by the borders of

the checkerboard images for the sake of convenience. In real grid or checkerboard images, this should be avoided in order to limit the negative effect of aliasing, which potentially induces parasitic fringes to appear in displacement and strain distributions. Rotating the regular pattern with respect to the grid of pixels of the camera sensor is a solution to get rid of this effect, as discussed in [27] in the case of grid patterns. No aliasing was observed in the present case probably because we considered synthetic checkerboard images obtained with pure sine functions in the examples, so this issue is not addressed here. The interested reader can find in [6, 11, 24] typical real and synthetic checkerboard images as well as close-up views to more easily visualize such patterns.

As explained above, the bias as defined here depends on the frequency of the signal. As a consequence, we consider checkerboard images deformed through a harmonic displacement field of uniform amplitude, the period of which linearly and gently increasing from the left to the right of the images. It is therefore expected to observe a decreasing attenuation (thus a decreasing bias) from the left to the right in the displacement field. The displacement being constant along the horizontal symmetry axis of the distribution, the attenuation of the displacement observed by each technique can be assessed by plotting the cross-section of the displacement along this line. This reference displacement field has been introduced in [28]. It has also been employed in recent studies dealing with the assessment of the metrological performance of full-field measurement systems [24] for instance, among which the DIC-challenge [29, 30]. It is plotted in Figure 4.
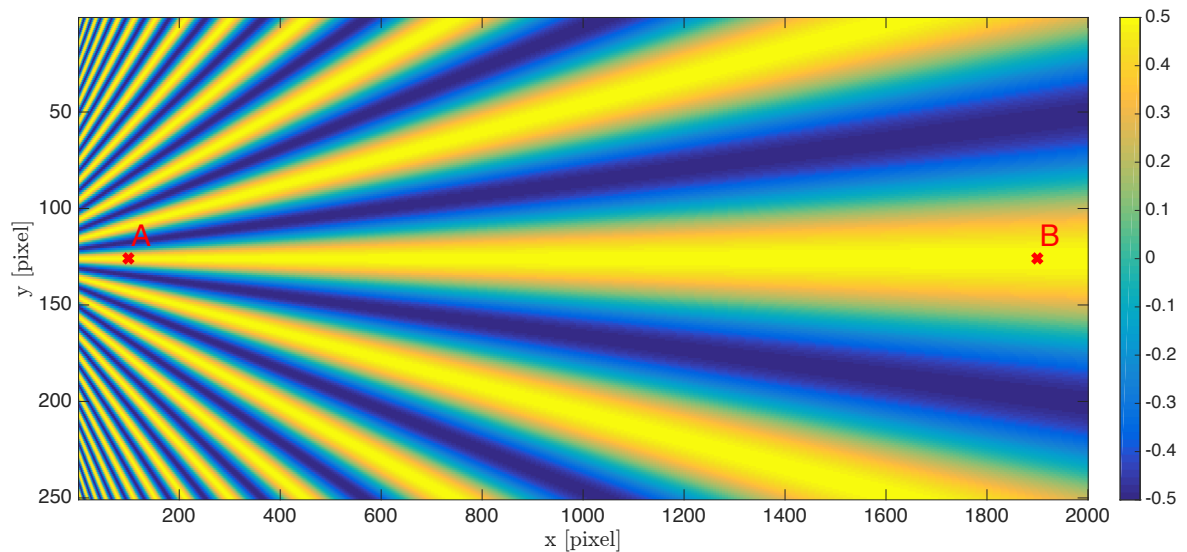

Figure 4: Distribution of the displacement used for the determination of the bias as a function of the period of the sine distribution of the displacement. Points A and B are the points for which the spectrum is represented in Section 2.2 in the case of WGPA.

This reference displacement is encoded in Equation 2, in which

$$\begin{cases} \Phi_x(x,y) = -\dfrac{2\pi}{p}u_x(x,y) = 0 \\ \Phi_y(x,y) = -\dfrac{2\pi}{p}u_y(x,y) = -\dfrac{2\pi}{p}B\cos\left(2\pi y/\left(p_{min} + (p_{max} - p_{min}) \times \dfrac{x}{L}\right)\right) \end{cases} , \qquad (3)$$

where $p_{min} = 10$ pixels, $p_{max} = 150$ pixels. L is the dimension of the image along x. The amplitude of the vertical displacement B is equal to 0.5 pixel, as in other studies where this type of synthetic displacement is used, [24] for instance. The period gently changing along the horizontal axis, the effect of the change in period under the window used for both WGPA and LSA can reasonably be neglected (the scale is different along the x- and y- axes in Figure 4). The spatial resolution for each technique is found by fixing first a value for the bias denoted by λ. The spatial resolution d is then deduced by finding the value of the period of the distribution returned by each technique, for which the amplitude of the distribution is equal to $(1 - \lambda)u_0$. This progressively becomes a standard procedure to estimate the bias, as in Ref. [31, 26, 32] for DIC, and in [33, 28, 24] for LSA. As mentioned in [9, 10], a closed-form expression is available for the prediction of the spatial resolution as a function of λ for LSA. It is however not used here in order to keep the same procedure to find the bias for GPA and WGPA, for which no such predictive formula exists, and LSA.

3.2   Displacement resolution

The displacement resolution σ_u is assessed by considering synthetic checkerboard images affected by noise, and observing how this noise propagates through each of the procedures used to find the phase, and eventually the displacement with Equation 1. In real images, noise is signal-dependent (thus heteroscedastic), which means that its standard deviation $\sigma_{image}(x,y)$ depends on the light intensity $s(x,y)$. This phenomenon is modeled by considering that the variance linearly depends on the gray level [34]. Thus

$$\sigma_{image}(x,y) = \sqrt{as(x,y) + b}, \qquad (4)$$

where a and b are parameters which depend of the camera. We used such a noise in the present work, with $a = 8.4547$, $b = -35332$. These values correspond to the parameters identified in [35] for a real 12-bit camera. Such a noisy checkerboard image was considered in the present study, which leads for each technique to displacement fields also affected by noise. For each technique, the displacement resolution σ_u is estimated by considering the standard deviation of the difference between the displacement estimated with noisy and noise-free images.

4   Results

### 4.1   Influence of various settings on the results

We examine first the displacement resolution obtained with the different techniques. GPA is investigated first.

10

4.1.1 GPA

Obtained results depend on two parameters in this case, namely the shape of $\mathcal{Z}_f$ and k defined in Section 2.1. Various choices are possible for these quantities but all the combinations cannot reasonably be investigated. Concerning $\mathcal{Z}_f$, this zone shall be large enough to contain the points where the Fourier coefficients of the spots are the highest in amplitude, but small enough to avoid any overlap with other spots such as those corresponding to the harmonics. In addition, enlarging $\mathcal{Z}_f$, especially toward the high frequencies, means that the result becomes more sensitive to noise. Figure 5-a shows the amplitude spectrum of an undeformed 251×2001 checkerboard image, each square of the checkerboard being encoded with 3 pixels along each direction. Equation 2, in which Φ_x and Φ_y are defined in Equation 3, is used to deform the checkerboard image. The horizontal and vertical directions of the amplitude spectrum are normalized. Hence the normalized frequencies along x and y both lie between -0.5 and 0.5. These normalized frequencies are not reported in the subfigures to more specifically focus on the pattern of the spectra themselves. Four sharp spots located along the ± 45 degrees are clearly visible in Figure 5-a, at the crossing points between the horizontal and vertical lines. It is worth mentioning that we are here in an idealized case, for which no harmonic is visible. These sharp spots become larger when the checkerboard image is deformed, as illustrated in Figure 5-b. It can be seen that the pattern around the peaks is not as simple as the limited number of points visible at the crossing between the vertical and horizontal lines in Figure 5-a. The question here is to define $\mathcal{Z}_f$ that shall be kept to perform GPA, and this definition obviously influences the quality of the final result. It is therefore discussed by considering two various zones $\mathcal{Z}_f$, which are represented in Figures 5-c and -d. They are named respectively small box and big box in the following.

Figure 6-a and -b show the displacement fields obtained when applying GPA with each of the two boxes but no clear difference is visible to the naked eye. Figure 6-c shows the cross-section of these two maps along their horizontal axis of symmetry. Slight fluctuations are visible on the right-hand side for the small box. Fluctuations with higher amplitude are also visible in both cases on the left-hand side, where the frequency is the highest. These fluctuations are however more limited with the large box, which is certainly due to the fact that higher frequencies being taken into account in the second case, reconstructing the high-frequency waves is easier. Changing the size and shape of $\mathcal{Z}_f$ would automatically lead to different results. This result illustrates therefore that choosing the size and shape of $\mathcal{Z}_f$ is quite arbitrary. In the following, we stick with the large box shown in Figure 5-d and discuss noise filtering by thresholding the Fourier coefficients involved in $\mathcal{Z}_f$.

In case of noisy data, the spectrum is affected and so the phase distributions. The spectrum of a noisy image of the deformed checkerboard image discussed above is depicted in Figures 5-e . The model for the noise is that described in Section 3.2. Comparing Figures 5-b and -e enables us to see the impact of noise. Indeed some small features of the spectrum around the spots are lost when the images are noisy. k defined for GPA in Section 2.1 directly governs the number of non-nul Fourier coefficients kept in the calculation of the displacement. The noise is expected to be more and more filtered as k increases since the number of non-nul Fourier coefficients decreases with this parameter. The question is however to know to which extent the actual details are negatively impacted, since representing the details relies on the highest frequencies in the spectrum. This contradictory effect (i.e. decreasing noise amplitude on the one hand, impairing the details on the other hand) is illustrated in Figure 7, where
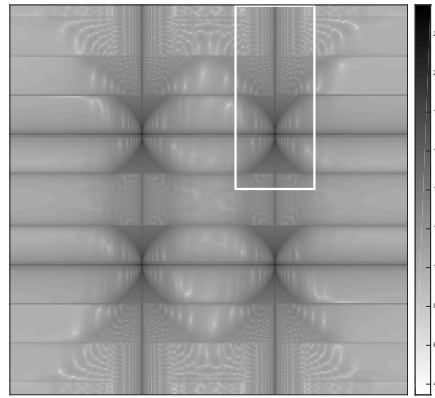
11
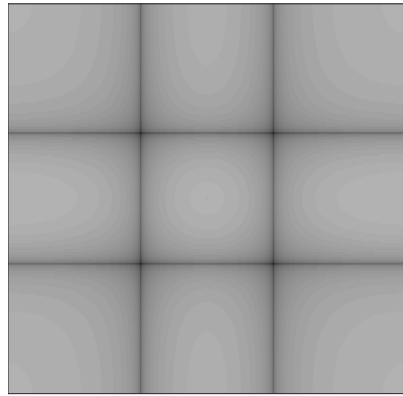
(a) spectrum of noiseless
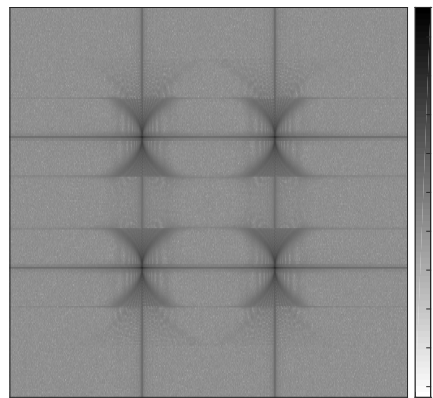undeformed checkerboard
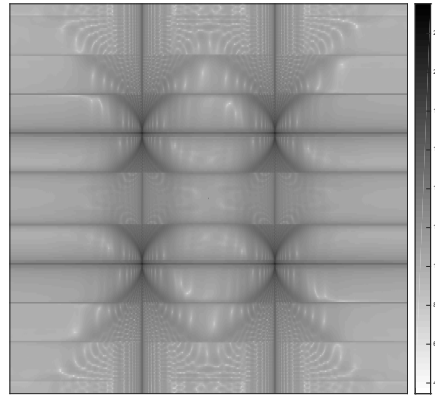
(b) spectrum of noiseless
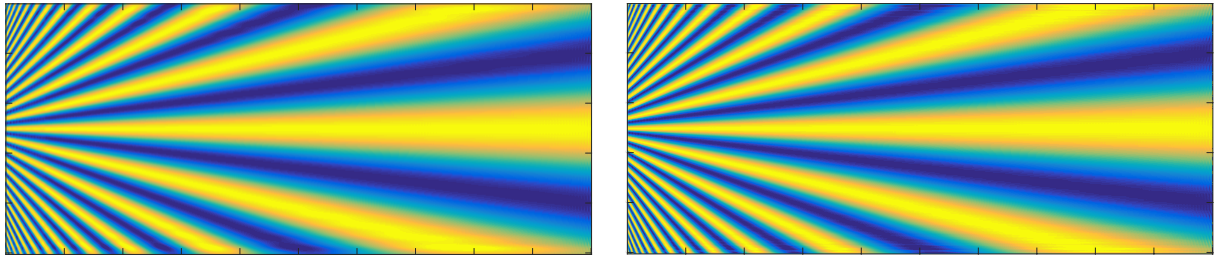deformed checkerboard
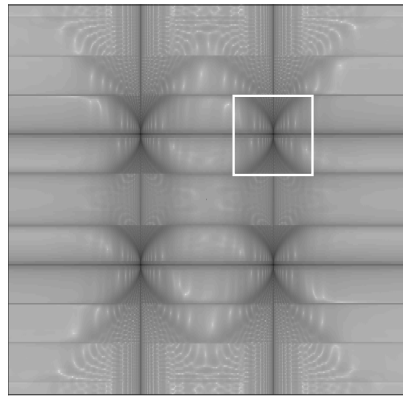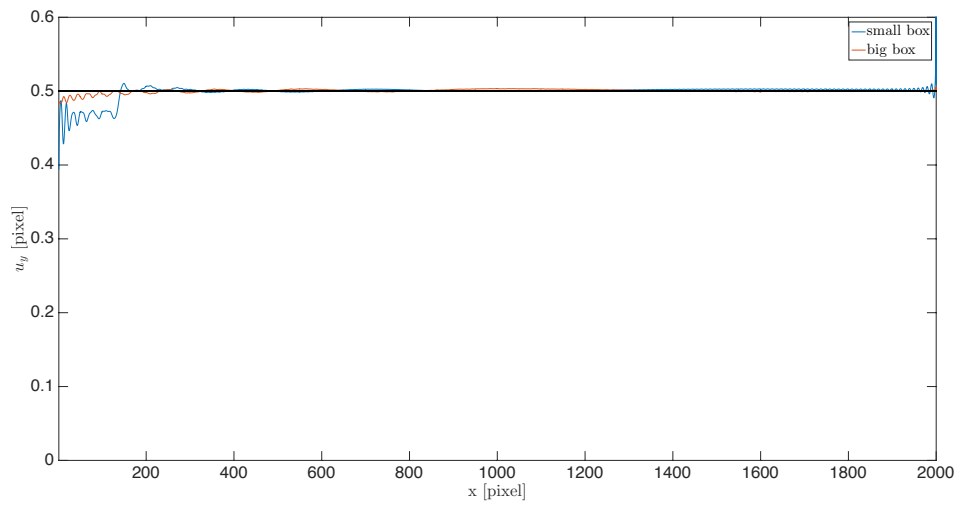
(c) small box

(d) large box

(e) spectrum of noisy deformed checkerboard
(to be compared with b-)

Figure 5: Amplitude spectrum of a checkerboard image and two different dimensions for zone $\mathcal{Z}_f$ selected to perform GPA. These spectra are obtained with noiseless ((a) to (d)) and noisy (e) checkerboard images.

12

(a) displacement field retrieved
with the large box

(b) displacement field retrieved
with the small box

(c) cross-section of the displacement field retrieved with both boxes

Figure 6: Displacement field obtained with GPA. $\mathcal{Z}_f$ is successively equal to the large and small box shown in Figure 5 above

the vertical displacement map retrieved for various values of k is represented. For k lower than 30%, no real effect can be seen to the naked eye. For higher values, the displacement maps become blurred, with a parasitic effect as k increases. This parasitic effect, which is mainly visible near the border, corresponds to a Gibbs effect. It is certainly due to the fact that abruptly zeroing a high number of Fourier coefficients is too rough a filtering procedure. More sophisticated approaches should be investigated to limit this phenomenon, but this is out of the scope of this paper.

The effect of the value of k is more visible in Figure 8, where the cross-section of the displacement distribution along the axis of symmetry is plotted for k lying between 0 and 50%. As expected, filtering becomes more and more efficient as k increases, but Gibbs effect affects the distribution near the borders of the figure. The best tradeoff seems to be $k = 30\%$ in this particular case.

The bias (or systematic error) affecting the results can be assessed by considering the difference between displacement field retrieved by the technique from noiseless images, and the reference displacement field. This quantity is denoted by $\delta u_y^i, i = \mathsf{GPA}, \mathsf{WGPA}, \mathsf{LSA}$, which can also be regarded as a residual. We focus here on the displacement along the y-direction (see Figure 4), the displacement along x being theoretically null. Thus

$$\delta u_y^i = u_y^i - u_y^{ref}, \quad i = \mathsf{GPA}, \mathsf{WGPA}, \mathsf{LSA}. \tag{5}$$

Figure 9 (a) and (b) shows typical $\delta u_y^{\mathsf{GPA}}$ distributions for two different typical settings. The Gibbs effect is clearly visible for the settings used in subfigure (b). A slight bias is also visible in these maps. It is all the greater as the frequency is high, which is certainly due to the fact that high frequencies are progressively lost when coefficient k used to threshold the frequencies increases. It is worth remembering that the bias discussed here represents, regardless of the Gibbs effect, the effect of a convolution with a kernel whose characteristics depend on the technique under consideration. This effect is however expected to be negligible with GPA, as discussed in Section 2.4, and this point is verified in this example.

4.1.2 WGPA

As explained in Section 2.2, WGPA is a localized version of GPA since the latter technique is applied pixelwise, on small zones $\mathcal{Z}_r$ surrounding any pixel of the checkerboard image. Since the corresponding spectra are defined pixelwise, they are also expected to change pixelwise. As an example, Figure 10 shows two spectra obtained at two different points A and B of the deformed checkerboard image. These points are reported in Figure 4. Their coordinates (x,y) are $\mathsf{A} : (100, 126)$ and $\mathsf{B} : (100, 1900)$. The first point corresponds to a high-frequency reference displacement, the second to a low-frequency one. $\mathcal{Z}_r$ is a Gaussian window. Its standard deviation is equal to 6 pixels to be consistent with the results of LSA discussed in the next section. The apparent size of the Gaussian window is a circle of diameter $6 \times \sigma = 24$ pixels according to the $3 - \sigma$ rule [36].

In Figure 10, it can be seen that both spectra globally have the same aspect, which is here more simple than the aspect of the spectrum of the deformed checkerboard image obtained for GPA, since compared to the whole image, a much lower number of frequencies is involved in the discrete Fourier transform. Indeed, we have here a central spot surrounded by four spots located along the diagonals. These four spots are elongated along the vertical direction for the point located on the left-hand side of the displacement maps, thus for the highest
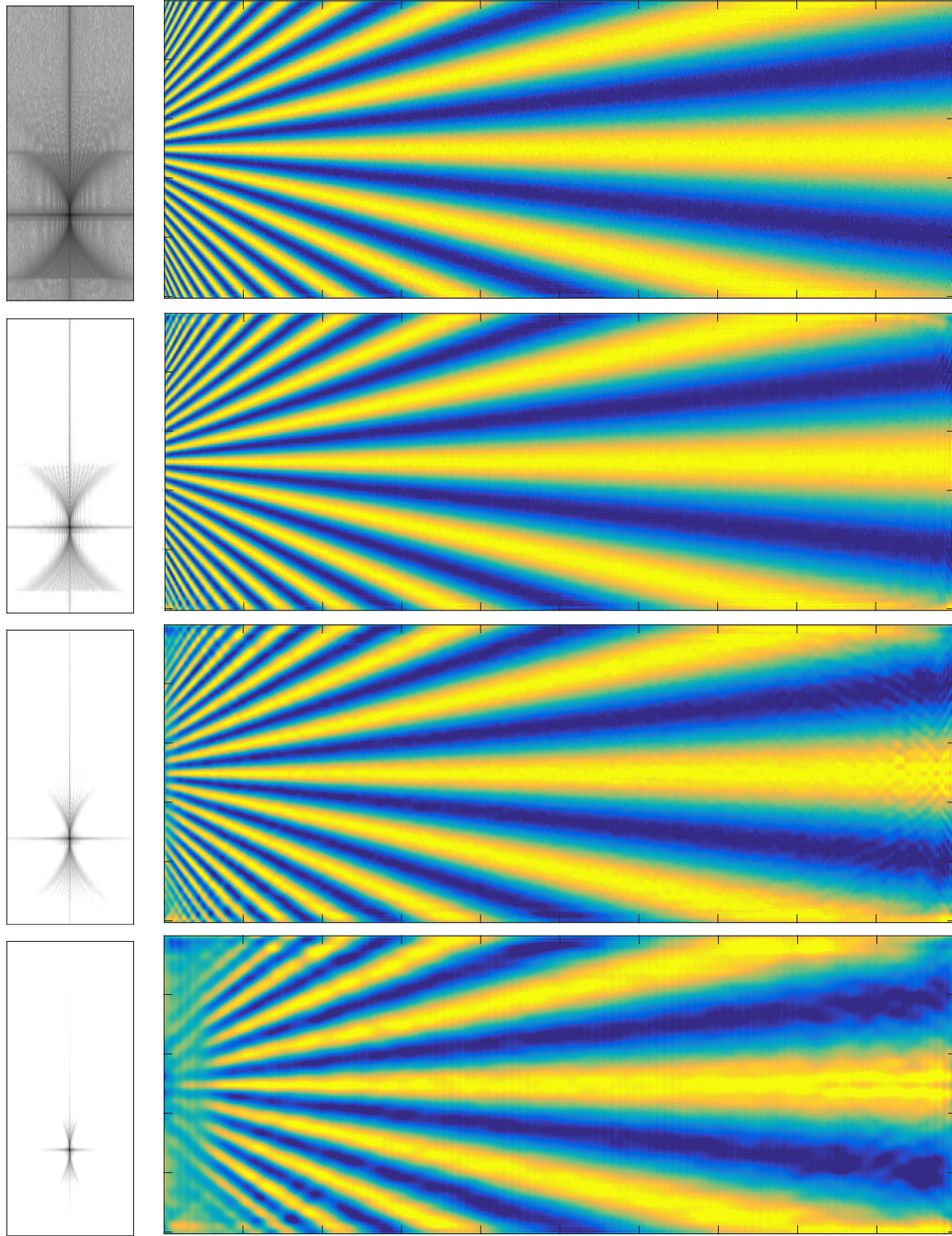
Figure 7: Left: closeup view of the box kept for the calculation in the amplitude spectrum. Right: corresponding displacement maps u_y for k=0, 30, 40, 50% from the top to the bottom (number of Fourier coefficients: 46,846; 10,340; 4,769; 1,274, respectively). The details are progressively lost and Gibbs effect occurs when k increases.
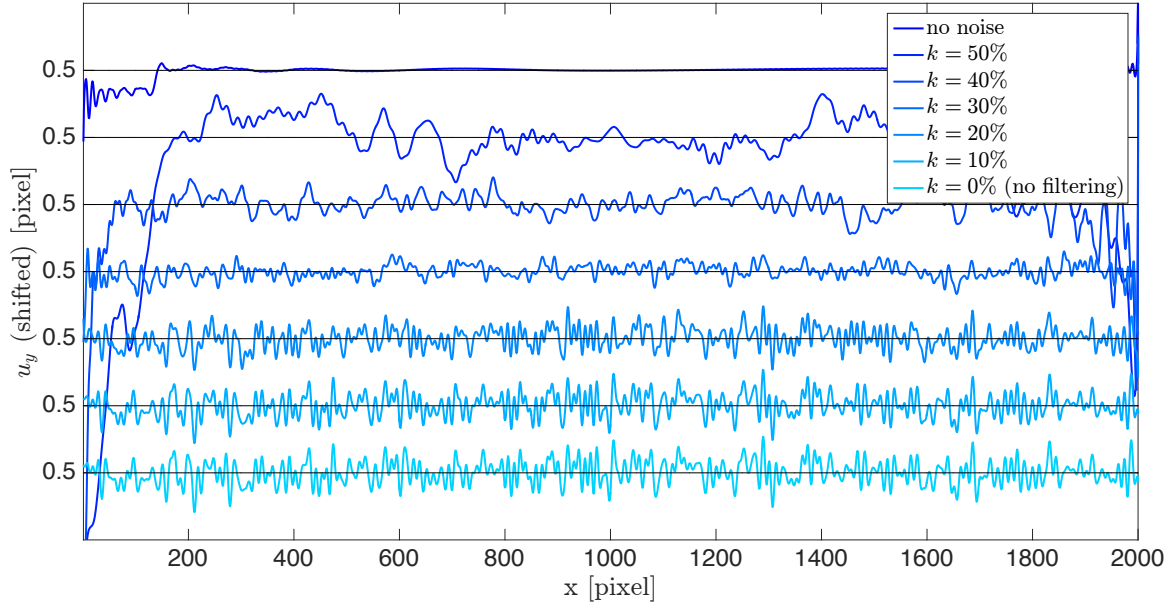
Figure 8: Cross-section of the displacement field along the horizontal axis of symmetry ($y = 126$ pixels) for various values of k. The reference value is 0.5 pixel in all cases but the curves are shifted vertically by 0.1 pixel in order to improve the readibility of the results.
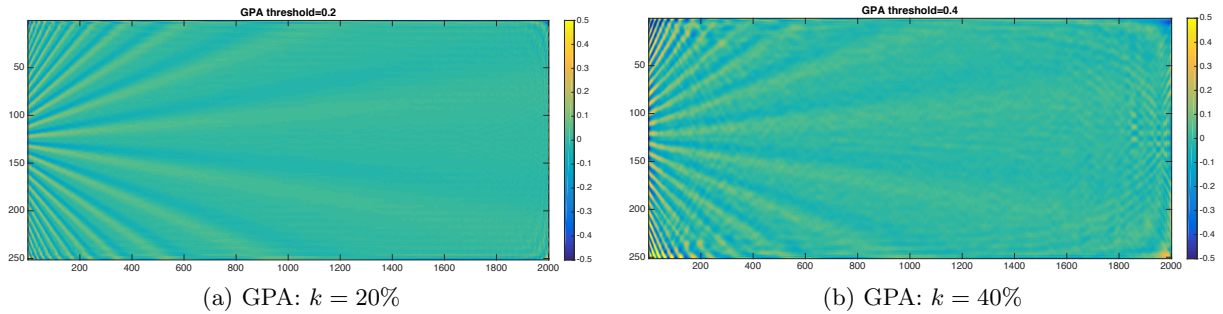

(a) GPA: $k = 20\%$

(b) GPA: $k = 40\%$

Figure 9: Maps of residual $\delta u_y^{\mathsf{GPA}}$ obtained for two typical values of k.

16

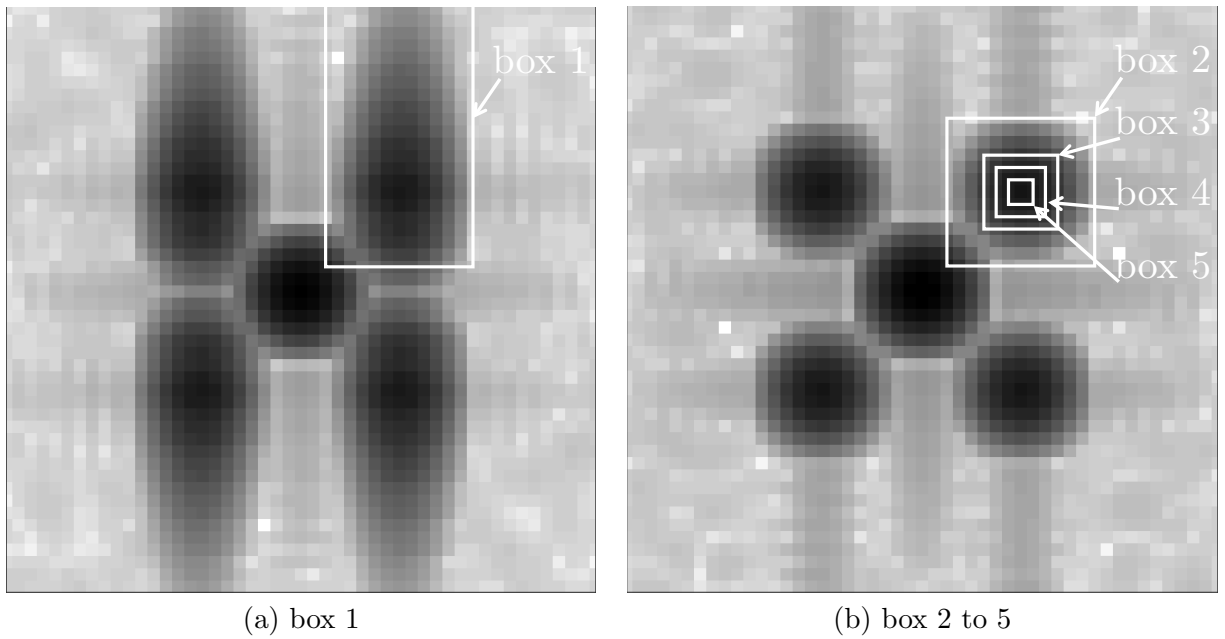(a) box 1   (b) box 2 to 5

Figure 10: Typical spectra obtained at two different points of the checkerboard localized at Point A (100,126) in (a), and at Point B (1900,126) in (b). $\mathcal{Z}_r$ in a Gaussian window (standard deviation: 6 pixels). Box 1 chosen for $\mathcal{Z}_f$ covers the spot in -a. Boxes 2 covers the spot in b-. Boxes of decreasing size (boxes 3 to 5) are also considered in b-.

spatial frequency (Point A), while they look like circles for the second point corresponding to the lowest spatial frequency (Point B). Indeed, the limited size of $\mathcal{Z}_r$ automatically reduces the frequency range activated to locally describe the phase distribution over this zone. The corresponding spectra are then automatically less rich in details. As for GPA, choosing at best $\mathcal{Z}_f$ is quite challenging. Indeed this zone should ideally include the spot surrounding the peak corresponding to the nominal frequency of the checkerboard, but the shape of the spot potentially changes from one zone to another of the image. Considering one quater of the spectrum (but excluding from this quarter the portion of the central spot of the spectrum) could be considered as the easiest solution, but this choice is too conservative, since it could for instance be affected by the presence of harmonics. In order to discuss the impact of this choice, we consider first two boxes defining $\mathcal{Z}_f$, namely box 1 in Figure 10-a and box 2 in Figure 10-b. Indeed a large one is necessary on the left to cover the whole spot since it is elongated along the vertical direction, while a smaller box is sufficient for the spot on the right. Choosing the large box is conservative and would cover all the cases in the present example, the black spot progressively decreasing in size from the left to the right of the image. As a general remark, reducing the size of the box reduces the number of frequencies involved in the description of the sought displacement. This progressively causes a bias to appear when $\mathcal{Z}_f$ does not cover the whole spot, and this bias is all the more pronounced as the size of $\mathcal{Z}_f$ decreases. On the other hand, the noise level is expected to increase as $\mathcal{Z}_f$ increases in size. In order to illustrate the effect of the size of the box on the noise level in the retrieved displacement field as well as on the "damping" of the signal as a function of the frequency of the sought displacement, we show in Figure 11 the cross-section of such fields obtained by processing a pair of synthetic checkerboard images. The reference one is the synthetic checkerboard presented above, the second one is the same checkerboard, but modulated with the phase distribution corresponding to the displacement shown in Figure 4. The five different boxes of decreasing size shown in Figure 10 are considered for this calculation. The curves obtained with and without noise clearly show that the noise level, as well as the bias affecting the highest frequencies in the measurement performed by using WGPA, is directly related to the size of $\mathcal{Z}_f$. Indeed, the smaller the area of $\mathcal{Z}_f$, the lower the noise and the higher the bias.

As for GPA, denoising can be performed by applying a threshold value for the Fourier coefficients involved in $\mathcal{Z}_f$. This threshold value is governed by k. Only the coefficients higher than this threshold value are then kept in the determination of the displacement field. Considering all the combinations between the choice of $\mathcal{Z}_f$ and k is not possible, so we only illustrate this point by two typical examples in Figures 12-a (box 1 and $k = 40\%$) and -b (box 5 and $k = 40\%$)

Compared to the preceding case of GPA (see Figure 9), the main remark is that the amplitude of this bias increases from the right to the left, thus when going to the highest frequencies, which illustrates the effect of convolution mentioned in Section 2.4 above. The nature of the kernel is however not explicitly given in the literature for WGPA. Thus, apart from saying that the effect of this convolution in all the more pronounced as the size of $\mathcal{Z}_f$ decreases (while containing the peak of the spot), it is difficult to analyze further convolution and potential deconvolution procedure in this case.

18
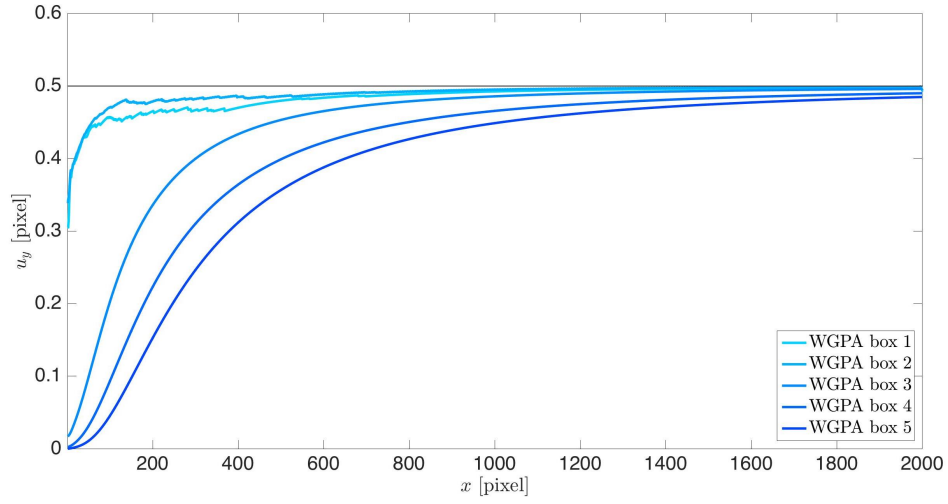
(a) with noiseless checkerboard images
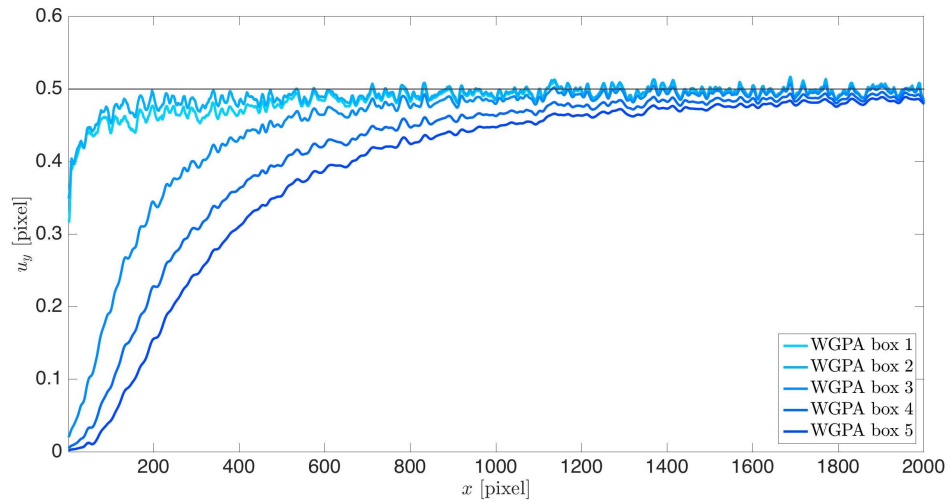
(b) with noisy checkerboard images

Figure 11: Cross-section of the displacement field retrieved by WGPA by considering the different boxes shown in Figure 10 along with the result obtained with LSA.
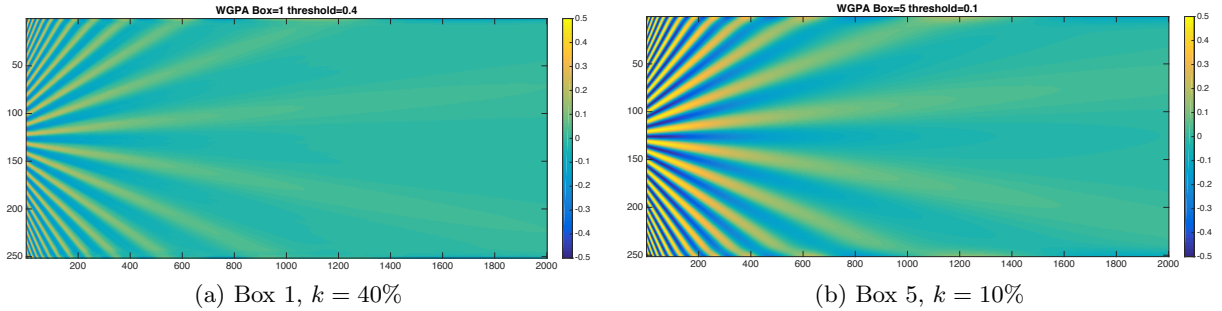
(a) Box 1, $k = 40\%$ (b) Box 5, $k = 10\%$

Figure 12: Maps of residual $\delta u_y^{\mathsf{WGPA}}$ obtained for two different zones $\mathcal{Z}_f$ (Box 1 and Box 5), and two typical values of k.

4.1.3 LSA

The ultimate setting for WGPA corresponds to the case for which $\mathcal{Z}_f$ reduces to one value only in the Fourier domain, namely the value corresponding to the peak (see Appendix 1). This peak theoretically corresponds to the nominal frequency of the lines of diamonds which can be observed by considering the checkerboard along its ± 45 degree directions. The curves obtained with LSA with and without applying the deconvolution algorithm discussed in Appendix 2 are reported in Figure 13. Three curves obtained in some particular cases of GPA are superimposed for comparison purposes. It can be seen that the curve obtained with LSA without deconvolution is nearly the same as the one obtained with WGPA with the smallest box (box 5). The small difference between the two curves is due to the fact that the frequency used with LSA is directly the nominal frequency of the grid, which is slightly different from the one corresponding to the peak in the Fourier domain.

The curve obtained after deconvolution is also reported in the same figure. It can be seen that its shape departs from the one of the other curves plotted in this figure. Indeed, the retrieved displacement abruptly tends to the reference value at the left-hand side of the figure, which means that the signal is retrieved without any bias up to a certain cutoff frequency discussed in [24]. The price to pay is an increase of the noise level affecting the results, which can be observed in the corresponding curve plotted in Figure 13-b. Compared to WGPA performed with the widest zones $\mathcal{Z}_f$ (boxes 1 and 2), it can be seen that the displacement retrieved with WGPA is closer to the reference value for the highest frequencies (on the very left of the curve), but under the cutoff frequency of the deconvolution procedure, no bias is observed with LSA, which is not the case for WGPA.

Figures 14 show the two $\delta u_y^{\mathsf{LSA}}$ distributions for LSA with and without deconvolution, respectively. The increase of the bias as the frequency increases is clear in Figures 14-a. The positive effect of deconvolution is illustrated in Figures 14-b since nearly no bias is observed up to a certain cutoff frequency for the displacement. The bias then suddenly increases when going beyond this cutoff frequency.

20
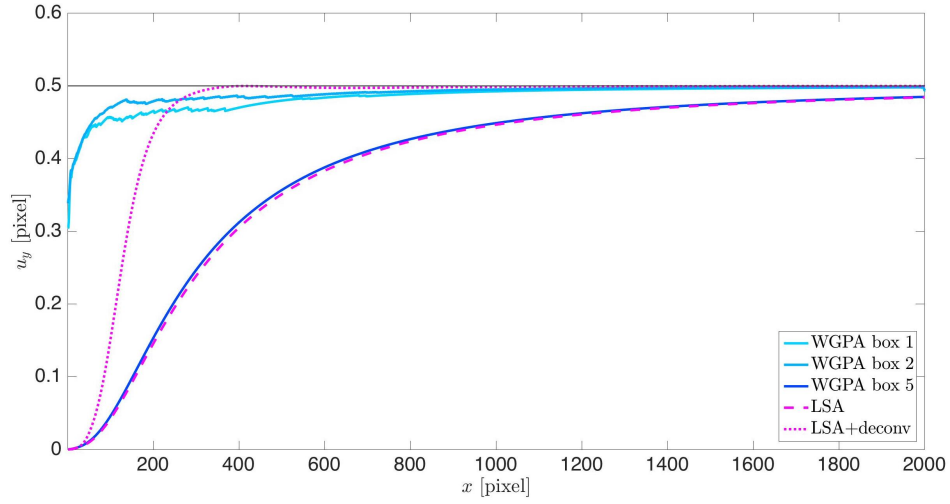
(a) with noiseless checkerboard images
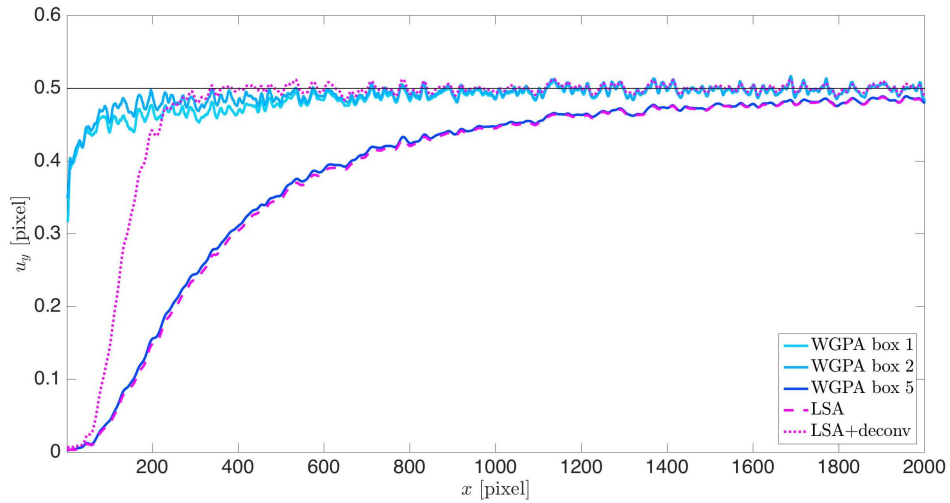
(b) with noisy checkerboard images

Figure 13: Cross-section of the displacement field retrieved by WGPA by considering the different boxes shown in Figure 10, along with the result obtained with LSA.
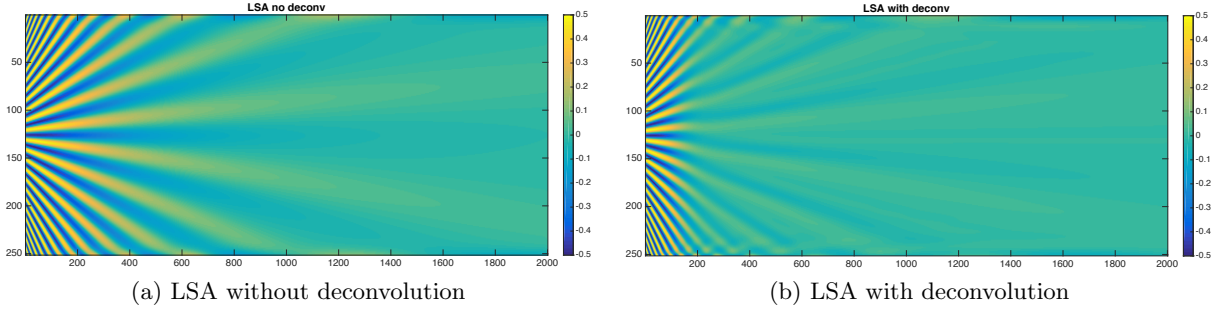
(a) LSA without deconvolution (b) LSA with deconvolution

Figure 14: Maps of residual $\delta u_y^{\mathsf{LSA}}$. The window w used with LSA is the same as the zone $\mathcal{Z}_r$ used with WGPA in Figure 12. This is a Gaussian enveloppe of standard deviation $\sigma = 6$ pixels.

4.2 Quantitative comparison between the metrological performance of the three techniques

In the preceding section, results obtained with the three techniques have been discussed qualitatively in turn. The objective is now to compare them from a quantitative point of view. Two points must however be taken into account for this comparison. First, some of the parameters such as the displacement resolution and the spatial resolution are linked, so this is more the relationship between these quantities that must be compared rather than these quantities individually. Second, depending on the technique, some parameters such as $\mathcal{Z}_f$, $\mathcal{Z}_r$ and k also influence the results.

We start first by investigating the displacement resolution obtained with the three techniques by using the following settings for these parameters:

- $\mathcal{Z}_f$ is the large box defined in Figure 5 for GPA, and successively all the five boxes shown in Figure 10 for WGPA;

- $\mathcal{Z}_r$ is a Gaussian window of standard deviation $\sigma = 6$ pixels for WGPA and LSA;

- parameter $k \in \{0\%, 10\%, 20\%, 30\%, 40\%, 50\%\}$ for GPA and WGPA. Higher values are not considered, the Gibbs effect becoming then too pronounced.

The results obtained in the different cases considered in this study are reported in Figure 15.

As a general remark, it can be said from the curves plotted in this figure that:

- Concerning GPA, σ_u decreases as k increases, which is logical.

- The same remark holds for WGPA for the largest zones $\mathcal{Z}_f$. Indeed, k has nearly no effect on the noise level in the displacement maps for the smallest zones $\mathcal{Z}_f$. The reason is that the lowest Fourier coefficients are directly removed in these latter cases. As already underlined in [13], the displacement resolution is lower (thus better) with WGPA than with GPA. The price to pay is however the fact that the highest frequencies are returned with an amplitude which is all the more reduced as the frequency is high.
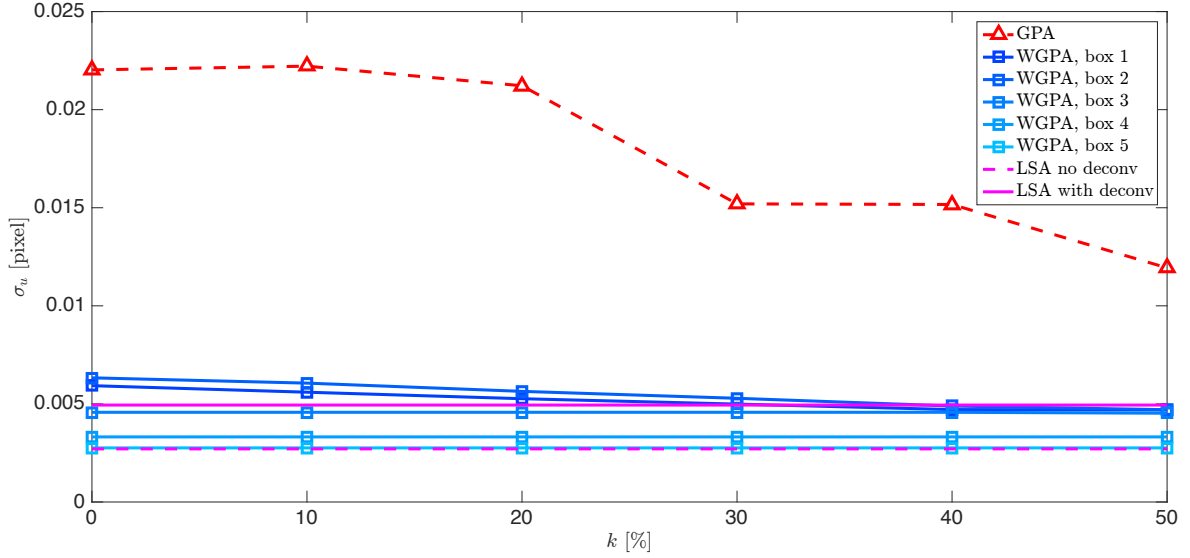
22

Figure 15: Displacement resolution obtained for the three techniques and various settings.

- The results obtained for WGPA with the smallest zone $\mathcal{Z}_f$ (i.e. Box 5) are about the same as those obtained for LSA. This is logical since LSA corresponds to the ultimate case of WGPA. It can be seen that deconvolution causes the noise level to increase in the maps. We have here approximately the same noise level with LSA after deconvolution as with WGPA used with Box 3.

At this stage, it could be tempting to conclude that GPA is not a good choice since it exhibits the worst displacement resolution. However this result does not take into account the spatial resolution of the different techniques. As suggested in [9], this quantity, denoted by d, can be estimated by considering the cross-section of the displacement field returned by a given technique along its horizontal line of symmetry, and by finding the period of the sinusoidal vertical displacement such that a bias λ equal to 10% is observed, see Section 3.1 and [26, 9, 37] for instance.

Figure 16 shows σ_u as a function of d for WGPA and various settings (fives possibilities for $\mathcal{Z}_f$, six values for k), along with the same quantity obtained with LSA performed with and without deconvolution. Concerning WGPA, it can be seen that σ_u decreases as d increases, as expected. It has been demonstrated and even experimentally observed in [38] that for LSA, σ_u is inversely proportional to d, which means that the different points should line up along a line with slope -1 if a log-log scale is used for the axes. Figure 15 shows that this property is not rigorously satisfied for WGPA when the settings for $\mathcal{Z}_f$ and k are changed. Concerning LSA, the two representative points illustrate the property discussed in [24], namely that deconvolution improves the spatial resolution (d diminishes) but causes the displacement resolution to increase. Concerning GPA, it is worth remembering that no convolution impacts the results provided by this technique, so d should theoretically be null. It means that the measured displacement is independent from one pixel to another. Filtering the results by increasing k slightly impairs this property, but d remains equal or close to zero with the

definition of d given above. This is illustrated by the left-pointing arrow reported in the figure. It can also be seen that the displacement resolution is significantly higher (thus worst) for GPA than for WGPA and LSA. This is the price to pay to obtain a measurement defined nearly pixelwise, without any influence of the actual displacement that occurs at the surrounding pixels.
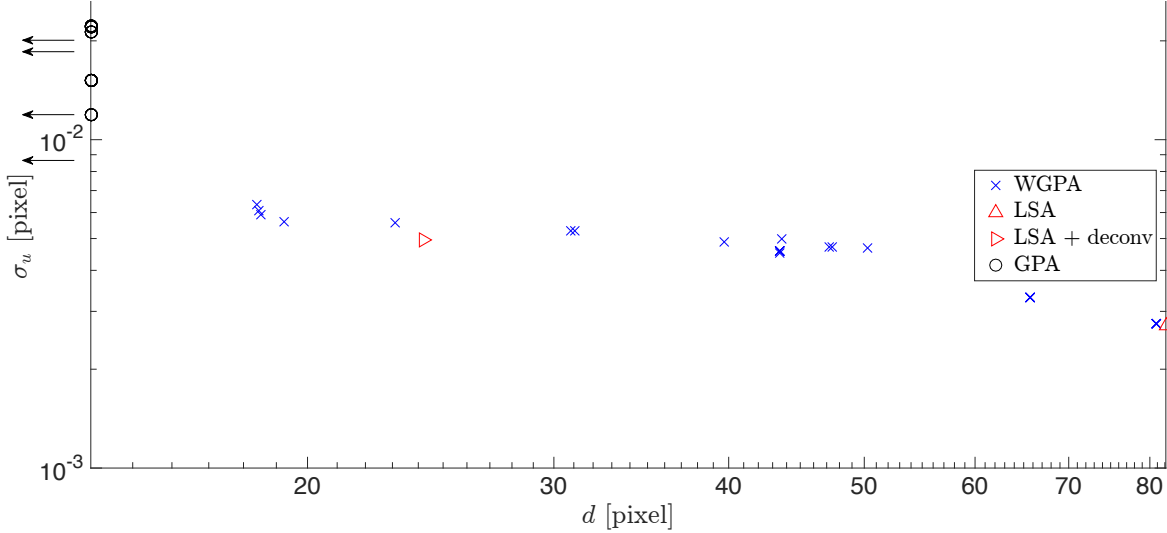

Figure 16: Displacement resolution σ_u as a function of the spatial resolution d.

In recent studies on LSA and DIC [39, 37], it is proposed to assess the compromise between spatial resolution and displacement resolution by considering the product between these two quantities. The reason is that this product has been demonstrated (respectively observed) to be constant for LSA (respectively for DIC) in [38] (respectively [39]). This product is denoted here by $\alpha = \sigma_u \times d$. It is referred to as the metrological performance indicator. The better the metrological performance, the lower the value of α. For comparison purposes, we propose here to calculate this product for the different settings used for WGPA as well as for LSA. A Gaussian window $\mathcal{Z}_r$ of standard deviation σ=6 pixels is used in both cases. GPA is not considered here, the spatial resolution being a priori null or close to zero for this technique. The obtained results are given in Figure 17.

The lowest values of α are obtained with WGPA and for the widest zones $\mathcal{Z}_f$. Increasing the value of k causes the displacement resolution σ_u to decrease, as discussed above, but this improvement is significantly counterbalanced by the impairment of the spatial resolution d. This is reflected by the product α, which increases as k increases. Adopting this metric, Box 4 and k=20% represent the best settings for WGPA. Interestingly, the lowest value of α for WGPA is 10% lower than its counterpart observed with LSA followed by deconvolution, which means that WGPA is slightly better than LSA for this particular setting. An important question is however to know the computational cost which is necessary to obtain these results. The answer is given in Figure 18, where typical computation times observed for the different techniques are reported. These time values are equal to the mean of the calculation times observed for all the different settings investigated for each technique in this study (6 different settings for GPA, 30 for WGPA, 1 for LSA). For GPA and WGPA, this computation time
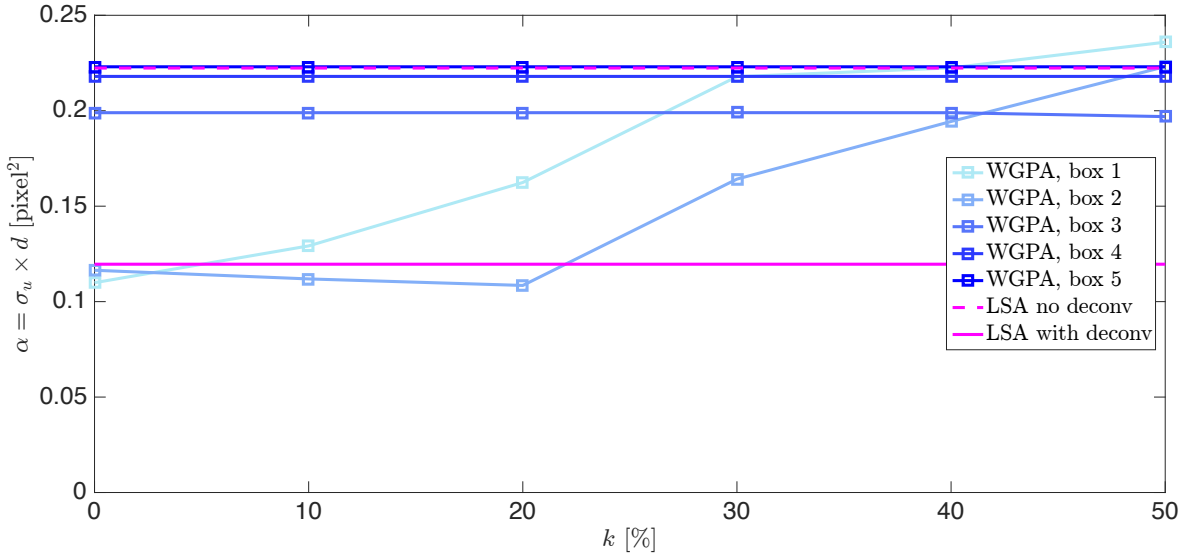
24

Figure 17: $\alpha = \sigma_u \times d$ for the three different techniques.

erratically fluctuates around the mean value from one case to another, so the mean value is a relevant global indicator. It is worth remembering that the images considered here are 2001×251 pixels^2 in size. The laptop computer used for these calculations is equipped with an Intel Core i7 @ 3.1 GHz and 16 Gb memory, and the number of iterations used for the iterative deconvolution procedure is set to 10, which is conservative according to [24]. Even though the reader should bear in mind that the Matlab programs corresponding to the different techniques are not optimized, and that these computation times strongly depend on the numerical resources of the computer that is used as well as of the size of the images, it can be seen that the computational time observed for the different techniques covers several decades between the fastest technique (GPA) and the slowest one (WGPA). In particular, the calculation time for LSA with deconvolution is noticeably different from that of WGPA since it is about 10 times lower in average. This ratio is exactly equal to 9.2 for the optimal settings, which have been observed here for WGPA, namely box 2 and $k = 20\%$, see Figure 17 above. There are two reasons for this difference between these techniques. First LSA relies on WFT carried out with one spatial frequency, namely $\sqrt{2}/\mathrm{p}$ [11], where p is the nominal pitch of the checkerboard, and this transform can be regarded as a convolution, which is advantageously performed in the Fourier domain since it becomes then a mere multiplication [10]. Second, the argument of the WFT directly provides the phase, so no inverse Fourier transform shall be applied before extracting the phase, which is not the case with WGPA, see Appendix 1. Note finally that the computation times observed for LSA and Digital Image Correlation are compared in [6].

5   Conclusion

Three spectral methods, namely the Geometric Phase Analysis (GPA), the windowed version of the Geometric Phase Analysis (WGPA), and the Localized Spectrum Analysis (LSA),
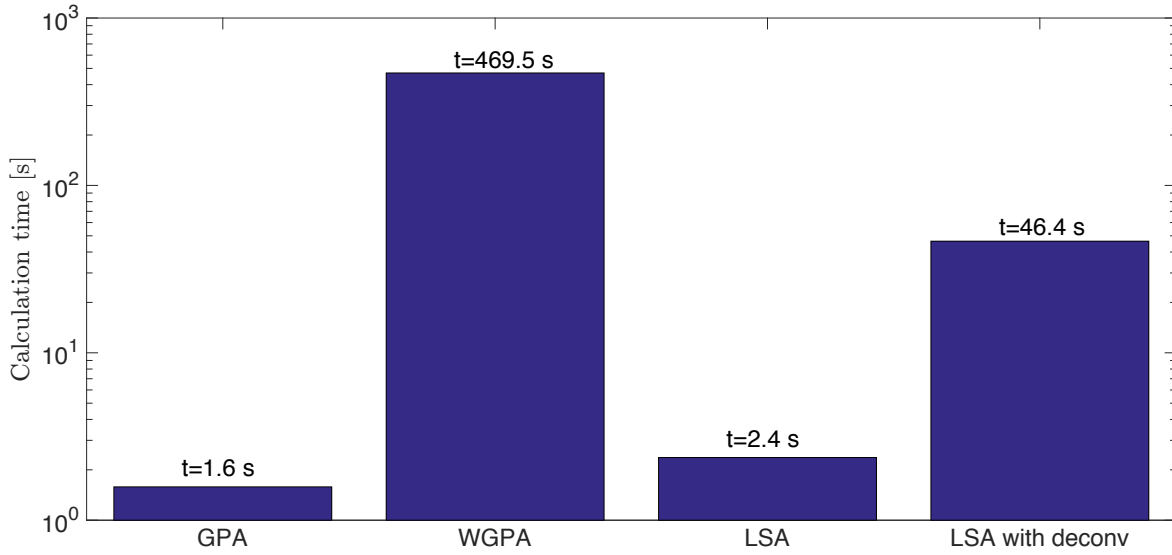
Figure 18: Typical computation time for the three different techniques. For each technique, this is the mean value observed for the different settings considered in this study. The size of the images processed here is 2001×251 pixels^2.

were used to process checkerboard images deformed with a synthetic reference displacement field. Such a pattern was studied because it exhibits the highest mean image gradient, which means that sensor noise propagation in the resulting displacement fields is minimum with this pattern. In addition, the pattern-induced bias is lower with this regular pattern than for random speckles. The three techniques were compared in terms of displacement resolution, spatial resolution and bias. It is shown that GPA is the fastest technique, but it is the most sensitive to image noise. WGPA significantly reduces the displacement resolution, but the price to pay is to induce a bias which manifests itself as a reduction of the amplitude of the highest frequencies involved in the displacement field. In addition, the zone to be selected in the spectra around or within the spots is somewhat arbitrary. The other feature of this technique is its high computational time, because it is equivalent to performing GPA on small zones of the image, which are as numerous as the pixels in the image if the determination of the displacement field is performed pixelwise. LSA followed by a suitable deconvolution procedure can easily be controlled, since the optimal settings is $\sigma = p$, as discussed in a preceding paper. Results are also easily characterized since there is a cutoff frequency above which all the frequencies involved in the sought displacement are returned without any bias. LSA has nearly the same metrological performance as WGPA when the latter is performed with optimal settings, but LSA is much faster than WGPA. This makes it a reasonable choice for the determination of displacement fields from deformed checkerboard images.

Appendix 1. Link between WGPA and LSA

The goal of this appendix is to give more details on WGPA and its link with LSA.

The Fourier transform of any integrable 2D function $f(\xi, \eta)$ is denoted here by $\widehat{f}(u, v)$. It is defined by:

$$\widehat{f}(u, v) = \iint_{\mathbb{R}^2} f(\xi, \eta) e^{-2i\pi(\xi u + \eta v)} \, d\xi \, d\eta. \tag{6}$$

The Dirac distribution centered at $(0, 0)$ is denoted by $\delta_{0,0}$.

A continuous bidimensional quasi-periodic pattern along the ξ- and η-axes can be modeled as:

$$s(\xi, \eta) = \frac{A}{2}\Big(2 + \gamma \cdot \ell(2\pi f\xi + \Phi_\xi(\xi, \eta)) + \gamma \cdot \ell(2\pi f\eta + \Phi_\eta(\xi, \eta))\Big), \tag{7}$$

where

- A is the global field illumination, considered constant;

- $\gamma \in [0, 1]$ is the contrast of the oscillatory pattern;

- the line profile ℓ is a 2π-periodic real function with a peak amplitude equal to 1 and average value 0;

- f is the nominal frequency of the carrier, the grid pitch being $p = 1/f$;

- $\Phi_\xi(\xi, \eta)$ and $\Phi_\eta(\xi, \eta)$ are the carrier phase modulations due to specimen surface displacements along the ξ- and η-axes respectively.

This bidimensional pattern may correspond to a checkerboard, but rotated by 45 deg with respect to the $x - y$ axes where Equation 2 is given, since a sine product becomes a sine summation in a coordinate system rotated by 45 deg. We also consider here a periodic function ℓ, so a sine function is a particular case and harmonics may also appear.

Let $\ell(\xi) = \sum_{k \in \mathbb{Z}} d_k e^{ik\xi}$ be the Fourier expansion of the 2π-periodic ℓ function. Since ℓ is a 0-mean real function, $d_0 = 0$ and for any k, d_k is the complex conjugate of d_{-k}.

As demonstrated in [27], the Fourier transform of s writes as follows:

$$\widehat{s}(u, v) = A\,\delta_{0,0} + \frac{\gamma A}{2} \sum_{k \in \mathbb{Z}} d_k \widehat{e^{ik\Phi_\xi}}(u - kf, v) + \frac{\gamma A}{2} \sum_{k \in \mathbb{Z}} d_k \widehat{e^{ik\Phi_\eta}}(u, v - kf). \tag{8}$$

Assuming that the partial derivatives of Φ_ξ or Φ_η are bounded, it is shown in [27] that the Fourier transform $\widehat{s}$ is made of several separated peaks, caused by the $\widehat{e^{ik\Phi_\xi}}$ and $\widehat{e^{ik\Phi_\eta}}$, centered at multiples of the frequency f along the ξ- and η-axes. This property explains the aspect of the spectrum shown in Figures 1 and 2 or in the experiments of Section 4. As explained in Section 2.1.1, GPA consists in applying first a band-pass filter which selects the frequency components inside $\mathcal{Z}_f$, and in shifting the result toward the center. With the notations of Equation 8, this process gives:

$$\widehat{s} \cdot \chi_{\mathcal{Z}_f}(u + f, v) = \frac{\gamma A}{2} d_1 \widehat{e^{i\Phi_\xi}}(u, v). \tag{9}$$

where $\chi_{\mathcal{Z}_f}$ is the characteristic function of the set $\mathcal{Z}_f$ (its value is 1 on this set, and 0 outside). In this calculation, we consider that $\mathcal{Z}_f$ is only made of components from the set of frequency components of $\widehat{e^{ik\Phi_\xi}}$. See [27] for further details and a thorough discussion of this hypothesis.

The argument of the inverse Fourier transform of this latter quantity therefore gives the phase distribution, up to an additive constant equal to the argument of the complex number d_1.

In the windowed version of GPA (namely WGPA), the Fourier transform is replaced by the windowed Fourier transform in the preceding equations. This simply amounts to multiplying s by a moving window w centered at a point of interest. We keep on denoting by $\widehat{f}$ the windowed Fourier transform of the bidimensional signal f.

We show in the remainder of this appendix that LSA can be seen as a special case of WGPA. Indeed, LSA simply consists in taking the argument of the value at $(f, 0)$ of the windowed Fourier transform of s. Assuming as above that the spectrum peaks are separated, Equation 8 gives:

$$\widehat{s}(f, 0) = \frac{\gamma A}{2} d_1 \widehat{e^{i\Phi_\xi}}(0, 0).$$ (10)

$\widehat{e^{i\Phi_\xi}}(0, 0)$ is simply the convolution of the moving window w and $e^{i\Phi_\xi}$. We have shown in [23] that, under mild assumptions, the argument of $\widehat{s}(f, 0)$ is the convolution of w and Φ_ξ, up to the additive constant term discussed above. In the same way, the argument of $\widehat{s}(0, f)$ gives the convolution of Φ_η with w.

Now, considering WGPA with $\mathcal{Z}_f$ restricted to $\{(f, 0)\}$, we obtain:

$$\widehat{s} \cdot \chi_{\mathcal{Z}_f}(u + f, v) = \frac{\gamma A}{2} \widehat{e^{i\Phi_\xi}} \delta_{0,0}(u, v).$$ (11)

The inverse (windowed) Fourier transform of this quantity is thus the convolution of $e^{i\Phi_\xi}$ and w. Indeed, the transform of a product is a convolution and the inverse windowed Fourier transform of the Dirac distribution is the moving window w. Hence taking the argument gives the convolution of Φ_ξ with w.

The main practical consequence of this result is that with LSA and contrary to WGPA, it is not necessary to explicitly calculate an inverse windowed Fourier transform: in order to obtain the phases, it is sufficient to take the argument of $\widehat{s}(f, 0)$ to obtain the same estimation of the phase Φ_ξ as with WGPA used in the special case characterized by $\mathcal{Z}_f = \{(f, 0)\}$. In both cases (LSA and WGPA in this special case), the retrieved phase is the convolution of the true phase with the analysis window, up to an additive constant. With the generic WGPA approach, thus in the case for which $\mathcal{Z}_f$ does not reduce to $\{(f, 0)\}$ only and covers the whole spot in the Fourier domain, an unbiased estimation of the phase is retrieved if Equation 9 holds true. In practice, however, the contribution of $\widehat{e^{i\Phi_\xi}}$ in Equation 8 may go beyond $\mathcal{Z}_f$, and the contribution of other terms may overlap this set, giving a bias resulting in a convolution of the true phase with a kernel that remains to be determined, but which is likely to vary spatially.

We can therefore conclude that LSA is a special case of WGPA where the band-pass filter is limited to the zone of interest $\mathcal{Z}_f = \{(f, 0)\}$. It can be noted that LSA retrieves a phase affected by a systematic bias because of the convolution of the phase and the analysis window w, contrary to the generic version of WGPA. However, LSA is less affected by noise than WGPA because it only consider a single frequency component where the useful signal dominates noise. In addition, it is possible to get rid of this bias up to a certain cutoff

frequency by applying the dedicated deconvolution algorithme recalled in Appendix 2 and detailed in [24].

Appendix 2. Deconvolution procedure for phases obtained with LSA

Using classic deconvolution algorithms to deconvolve displacement or strain maps obtained by LSA is not relevant because the results they provide are sensitive to noise [28]. A deconvolution algorithm accounting for the specificities of displacement and strain maps has been recently proposed in [24]. This algorithm consists in applying the following procedure

$$
\begin{cases}
\widetilde{\underline{\Phi}}^0 = \widetilde{\underline{\Phi}} \\
\widetilde{\underline{\Phi}}^{\text{it}+1} = \widetilde{\underline{\Phi}} - \delta\widetilde{\underline{\Phi}}^{\text{it}} \\
\text{with } \delta\widetilde{\underline{\Phi}}^{\text{it}} = \dfrac{1}{2} \sum_{i=\{\eta,\xi\}} \sum_{k,l=1}^{2} \widetilde{\Phi}^{\text{it}}_{i,kl} \, I_{kl} \, \underline{e}_i
\end{cases},
\tag{12}
$$

where $\widetilde{\Phi}^{\text{it}}_{i,kl}$ is the second derivative with respect to x_k and x_l. We denote by $\underline{\Phi}$ the vector whose components are the phases along directions η and ξ. It is estimated in practice by convolution of the map q by a second-order derivative kernel, chosen here as a classic "Mexican hat". η and ξ are the directions along which $\widetilde{\underline{\Phi}}$ is determined, here the two bisectors of the checkerboard [11]. I_{kl} is the second moment of the Gaussian kernel w. It is defined by

$$
I_{kl} = \iint_{(\eta_1,\eta_2)\in\Re^2} w(\eta_1,\eta_2)\eta_k\eta_l \, \mathrm{d}\eta_1 \, \mathrm{d}\eta_2.
\tag{13}
$$

The flowchart in Figure 19 sums up the deconvolution procedure.

For LSA applied on checkerboards, it has been observed in [24] that the maximum value of the standard deviation of the Gaussian σ that could be used as a kernel in the windowed Fourier transform was equal to the pitch of the checkerboard. Greater values cause the deconvolution algorithm to diverge for some frequencies, and should therefore be avoided.

Finally, it is worth recalling from [24] that deconvolution can be applied for a certain frequency range only. The benefit is to avoid amplifying the amplitudes of the signals corresponding to the highest frequencies in the signal, which often are due to noise and not to actual details. It means that deconvolution is applied only for the frequencies lower than a threshold value, which is possible by considering a notch filter in the Fourier domain while deconvolving the maps. It has been observed that choosing a threshold value equal to 0.1 pixel^{-1} leads to a significant reduction of the noise in the resulting maps, so this value for the threshold value is used in this study.
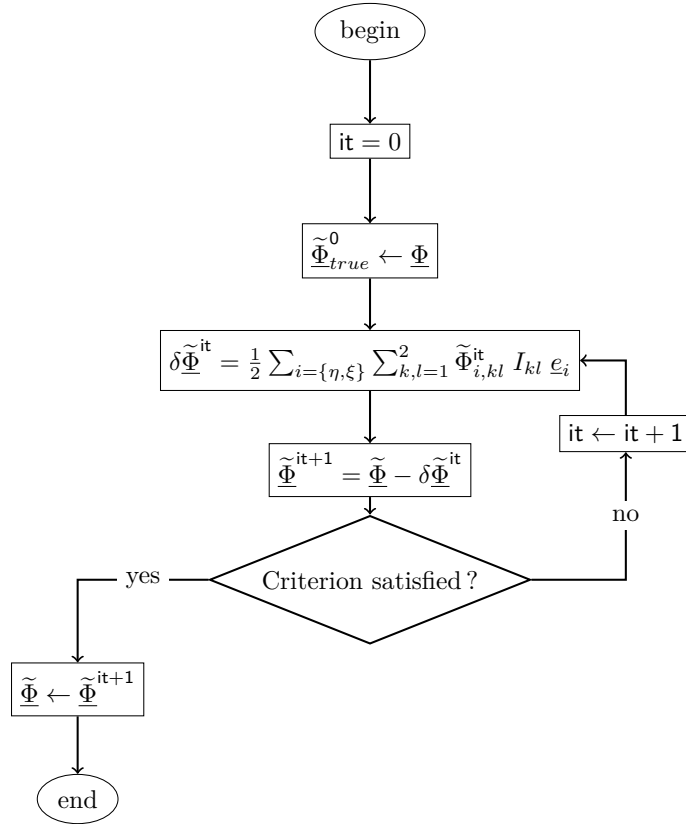
Figure 19: Flowchart of the deconvolution algorithm. In this study, the criterion used to stop the iterative calculation of the corrective term is the number of iterations, equal here to 10 according to [24].

References

[1] D. Lecompte, A. Smits, S. Bossuyt, H. Sol, J. Vantomme, D. Van Hemelrijck, and A.M. Habraken. Quality assessment of speckle patterns for digital image correlation. *Optics and Lasers in Engineering*, 44(11):1132–1145, 2006.

[2] S. Bossuyt. Optimized patterns for digital image correlation. In *Proceedings of the 2012 Annual Conference on Experimental and Applied Mechanics, Volume 3: Imaging Methods for Novel Materials and Challenging Applications*, 2013.

[3] G.F. Bomarito, J.D. Hochhalter, T.J. Ruggles, and A.H. Cannon. Increasing accuracy and precision of digital image correlation through pattern optimization. *Optics and Lasers in Engineering*, 91:73 – 85, 2017.

[4] J. Réthoré. A fully integrated noise robust strategy for the identification of constitutive laws from digital images. *Internation Journal for Numerical Methods in Engineering*, 84(6):631–660, 2010.

[5] B. Pan, Z. Lu, and H. Xie. Mean intensity gradient: an effective global parameter for quality assessment of the speckle patterns used in digital image correlation. *Optics and Lasers in Engineering*, 48(4):469–77, 2010.

[6] M. Grédiac, B. Blaysat, and F. Sur. On the optimal pattern for displacement field measurement: random speckle and DIC, or checkerboard and LSA? 2019. In revision.

[7] F. Sur, B. Blaysat, and M. Grédiac. On biases in displacement estimation for image registration, with a focus on photomechanics. 2019. Under review.

[8] S.S. Fayad, D.T. Seidl, and P.L. Reu. Spatial DIC errors due to pattern-induced bias and grey level discretization. *Experimental Mechanics*, 2019. Accepted, doi: 10.1007/s11340-019-00553-9.

[9] M. Grédiac, B. Blaysat, and F. Sur. A critical comparison of some metrological parameters characterizing local digital image correlation and grid method. *Experimental Mechanics*, 57(3):871–903, 2017.

[10] M. Grédiac, F. Sur, and B. Blaysat. The grid method for in-plane displacement and strain measurement: a review and analysis. *Strain*, 52(3):205–243, 2016.

[11] M. Grédiac, B. Blaysat, and F. Sur. Extracting displacement and strain fields from checkerboard images with the Localized Spectrum Analysis. *Experimental Mechanics*, 59(2):207–218, 2019.

[12] M. J. Hÿtch, E. Snoeck, and R. Kilaas. Quantitative measurement of displacement and strain fields from HREM micrographs. *Ultramicroscopy*, 74:131–146, 1998.

[13] X. Dai, H. Xie, and H. Wang. Geometric phase analysis based on the windowed Fourier transform for the deformation field measurement. *Optics and Laser Technology*, 58(6):119–127, 2014.

[14] S. Ri, M. Fujigaki, and Y. Morimoto. Sampling moiré method for accurate small deformation distribution measurement. *Experimental Mechanics*, 50(4):501–508, 2010.

[15] S. Ri and T. Muramatsu. Theoretical error analysis of the sampling moiré method and phase compensation methodology for single-shot phase analysis. *Applied Optics*, 51(16):3214–3223, 2012.

[16] S. Ri, T. Muramatsu, M. Saka, K. Nanbara, and D. Kobayashi. Accuracy of the sampling moiré method and its application to deflection measurements of large-scale structures. *Experimental Mechanics*, 52(4):331–3340, 2012.

[17] X. Dai, H. Xie, H. Wang, C. Li, Z. Liu, and L. Wu. The geometric phase analysis method based on the local high resolution discrete Fourier transform for deformation measurement. *Measurement Science and Technology*, 25(2):025402, 2014.

[18] Y. Surrel. Moiré and grid methods: a signal-processing approach. In Stupnicki J Pryputniewicz RJ, editor, *Interferometry'94: photomechanics*, volume 2342. SPIE, 1994.

[19] Y. Surrel and B. Zhao. Simultaneous u-v displacement field measurement with a phase-shifting grid method. In Stupnicki J Pryputniewicz RJ, editor, *Proceedings of the SPIE, the International Society for Optical Engineering*, volume 2342. SPIE, 1994.

[20] Q. Kemao. Two-dimensional windowed Fourier transform for fringe pattern analysis: Principles, applications and implementations. *Optics and Lasers in Engineering*, 45(2):304–317, 2007.

[21] Q. Kemao. Applications of windowed Fourier fringe analysis in optical measurement: a review. *Optics and Lasers in Engineering*, 66(2):67–73, 2015.

[22] F. Sur and M. Grédiac. Influence of the analysis window on the metrological performance of the grid method. *Journal of Mathematical Imaging and Vision*, 56(3):472–498, 2016.

[23] F. Sur and M. Grédiac. Towards deconvolution to enhance the grid method for in-plane strain measurement. *Inverse Problems and Imaging*, 8(1):259–291, 2014. American Institute of Mathematical Sciences.

[24] M. Grédiac, B. Blaysat, and F. Sur. A deconvolution algorithm to enhance displacement and strain maps obtained with DIC and LSA. *Experimental Mechanics*, 59(2):219–243, 2019.

[25] R.C. Gonzalez and R. E. Wood. *Digital Image Processing*. Pearson Education, 2009.

[26] L. Wittevrongel, P. Lava, S. V. Lomov, and D. Debruyne. A self adaptive global digital image correlation algorithm. *Experimental Mechanics*, 55(2):361–378, 2015.

[27] F. Sur, B. Blaysat, and M. Grédiac. Determining displacement and strain maps immune from aliasing effect with the grid method. *Optics and Lasers in Engineering*, 86:317–328, 2016.

[28] M. Grédiac, F. Sur, C. Badulescu, and J.-D. Mathias. Using deconvolution to improve the metrological performance of the grid method. *Optics and Lasers in Engineering*, 51(6):716–734, 2013.

[29] P. L. Reu, B. Blaysat, J. Helm, E. M.C. Jones, and M. Iadicola. Update on the DIC challenge 2.0 and the stereo-DIC challenge. In *SEM annual conference "Expanding the Boundaries of Mechanics", Reno, USA*, 2019. Proceedings of the conference.

[30] DIC challenge: http://sem.org/dic-challenge/.

[31] M. Bornert, F. Brémand, P. Doumalin, J.-C. Dupré, M. Fazzini, M. Grédiac, F. Hild, S. Mistou, J. Molimard, J.-J. Orteu, L. Robert, Y. Surrel, P. Vacher, and B. Wattrisse. Assessment of digital image correlation measurement errors: methodology and results. *Experimental Mechanics*, 49(3):353–370, 2009.

[32] J. Blaber, B. Adair, and A. Antoniou. Ncorr: Open-source 2D digital image correlation matlab software. *Experimental Mechanics*, 2015.

[33] C. Badulescu, M. Bornert, J.-C. Dupré, S. Equis, M. Grédiac, J. Molimard, P. Picart, R. Rotinat, and V. Valle. Demodulation of spatial carrier images: Performance analysis of several algorithms. *Experimental Mechanics*, 53(8):1357–1370, 2013.

[34] A. Foi, M. Trimeche, V. Katkovnik, and K. Egiazarian. Practical Poissonian-Gaussian noise modeling and fitting for single-image raw-data. *IEEE Transactions on Image Processing*, 17(10):1737–1754, 2008.

[35] F. Sur and M. Grédiac. Sensor noise modeling by stacking pseudo-periodic grid images affected by vibrations. *IEEE Signal Processing Letters*, 21(4):432–436, 2014.

[36] E. W. Grafarend. *Linear and Nonlinear Models: Fixed Effects, Random Effects, and Mixed Models*. Walter de Gruyter, 2006.

[37] B. Blaysat, J. Neggers, M. Grédiac, and F. Sur. Towards criteria characterizing the metrological performance of full-field measurement techniques. Application to the comparison between local and global versions of DIC. *Experimental Mechanics*, 2019. Accepted, doi: 10.1007/s11340-019-00566-4.

[38] M. Grédiac and F. Sur. Effect of sensor noise on the resolution and spatial resolution of the displacement and strain maps obtained with the grid method. *Strain*, 50(1):1–27, 2014. Paper invited for the 50th anniversary of the journal.

[39] M. Grédiac, B. Blaysat, and F. Sur. A critical comparison of some metrological parameters characterizing local digital image correlation and grid method. *Experimental Mechanics*, 57(6):871–903, 2017.